Supporting Information

Vapor Phase Synthesis of Metal Organic Frameworks on a Nanofibrous Aerogel Creates Enhanced Functionality

Vahid Rahmanian, Muhammed Ziauddin Ahmad Ebrahim, Seyedamin Razavi, Mai Abdelmigeed, Eduardo Barbieri, Stefano Menegatti, Gregory N. Parsons, Fanxing Li, Tahira Pirzada* and Saad A. Khan*

Department of Chemical & Biomolecular Engineering, North Carolina State University, Raleigh, NC 27695-7905, USA; E-mail: tpirzad@ncsu.edu; khan@eos.ncsu.edu

Characterization methods:

Density and porosity of the NFAs*:* The density (ρ) of the nanofiber aerogels (NFAs) was determined according to ISO 845:2006, which is a standard method for determining the density of cellular materials such as polymer foams and aerogels.[1,2] The mass of the aerogel sample was obtained by weighing it on a precision balance, and the volume was calculated from the radius (r) and height (h) of the cylindrical sample, which were measured using a Vernier caliper. The porosity (η) of the NFAs was then calculated using the following equation, where ρ_{NFA} is the density of the NFA and ρ_{NFs} is the bulk state density of the nanofibers.

$$\%\ Porosity = 100 \times \left(1 - \left(\frac{\rho_{NFA}}{\rho_{NFs}}\right)\right) \quad (1)$$

Surface Morphology and Element Detection: The morphology and surface composition of nanofibers and NFA were analyzed using Field Emission scanning electron microscopy (FESEM) equipped with energy-dispersive X-ray spectroscopy (EDX). The samples were prepared by sputter-coating with a 6-7 nm layer of Gold-Palladium. The detector was set to ETD in SE mode and the images were taken at an accelerating voltage of 2 kV and a current of 13 pA, while EDX analysis was conducted at 15 kV.

X-ray Diffraction (XRD): X-ray diffraction (XRD) was used to analyze the crystalline phases of the samples. The XRD measurements were performed using a PANalytical Empyrean X-ray diffractometer with a scan rate of 98 sec/step and a step size of 0.026 degrees. The XRD pattern of the ZIF-8 powder was simulated using the Mercury 3.10 software, and the crystallographic information file from the Cambridge Crystallographic Data Centre (CCDC 602542) was used for ZIF-8.

Brunauer-Emmett-Teller (BET) surface area: Nitrogen physisorption isotherms were measured using a Micrometrics 3Flex instrument. The Brunauer-Emmett-Teller (BET) method was used to calculate the surface area of the samples, which is a commonly used approach to determine the MOF (metal-organic frameworks) loading.[3] The BET surface area was calculated from Nitrogen adsorption isotherm between relative pressures of 0.01-0.1 at 77 K.

Fourier Transform Infrared (FTIR) Spectroscopy: The infrared spectra were collected using a Bruker Alpha Fourier-transform infrared (FT-IR) spectrophotometer equipped with an Attenuated Total Reflectance (ATR) accessory. The spectra were collected with 64 scans over a wavenumber range of 400-4000 cm^{-1} and a resolution of 0.5 cm^{-1}. The OPUS software was used for data collection and processing.

Thermogravimetric Analysis: Oxidative thermogravimetric analysis (TGA) of the samples was performed using SDT 650 by TA instrument. The test procedure consisted of three stages: i) heating at a rate of 10 ℃/min to 150 ℃, ii) a one hour hold to remove adsorbed species and volatiles, and ultimately iii) heating to 800 ℃ at a rate of 10 ℃/min. The test was performed in air at a flow rate of 50 ml/min and purging with Nitrogen at 100 ml/min.

Mechanical Testing: Dynamic compression/tension testing was performed on cylindrical samples of CDA-silica and CDA-silica@ZIF-8 NFAs using a Discovery Hybrid Rheometer (DHR3) with a 40 mm parallel plate geometry. The samples had a diameter of approximately 35 mm. Fatigue tests were conducted by applying ten loading-unloading cycles at a fixed strain at a rate of 100 μm sec^{-1}. The compressive stress and strain were calculated using the standard equations:

$$\sigma = \frac{F}{\pi r^2} \tag{2}$$

$$\varepsilon = \frac{h_0 - h_i}{h_0} \tag{3}$$

where σ is the stress, ε is the strain, F is the axial force, h_0 is the original height of the sample and h_i is the height of the sample at each time.

CO_2 adsorption - mechanism and kinetics

Adsorption mechanism: In the context of CO_2 capture, previous investigations have extensively utilized a range of characterization techniques to comprehensively evaluate ZIF-8 samples under various experimental conditions. These conditions encompassed distinct stages, including the initial state, the activated state, as well as the adsorbed and desorbed states. Through the application of techniques such as X-ray Diffraction (XRD), Scanning Electron Microscopy (SEM), and Transmission Electron Microscopy (TEM), a meticulous examination was carried

out, yet no discernible discrepancies emerged across the diverse testing phases. Notably, the foundational and bulk structure of these ZIF-8 specimens displayed a significant degree of resilience and stability throughout the entirety of the CO_2 adsorption experiments. This stability underscores the robust nature of ZIF-8 as a promising candidate for CO_2 capture applications. The utilization of the X-ray absorption fine structure (XAFS) technique distinctly revealed that the primary driving force behind CO_2 capture by the ZIF-8 pore structure arises from physical transformations. An advantageous aspect arising from the recognition of the physical interaction between these materials and carbon dioxide lies in the heightened energy efficiency demonstrated by the adsorption of CO_2 onto porous substrates. This approach proves more energy-efficient compared to the use of chemical absorbents for CO_2 capture, as the physical adsorption process requires lower energy input during the regeneration phase.[4]

Pseudo-first-order model: The pseudo-first-order model is frequently utilized to predict the adsorption behaviors of physical adsorbents such as zeolites, silica, and activated carbon.[5,6] Conversely, the pseudo-second-order kinetic model suggests that the adsorption process might involve significant chemical reactions, resulting in gases adhering to the adsorbent surface through covalent bonding. Since the interaction between CO_2 and ZIF-8 occurs through physical interaction, we employ the first-order model to predict the adsorption kinetics. The rate expression of the pseudo-first-order model throughout the entire adsorption process can be formulated as follows:

$$\frac{dq}{dt} = k_f \left(q_e - q_t\right) \qquad (S1)$$

where, q_e (mmol/g) and q_t (mmol/g) are the CO_2 adsorption capacity at equilibrium and at any time respectively for per mass of adsorbent, and k_f (min^{-1}) is the rate constant of first order adsorption.[7]

Boundary conditions:

$t=0$, $q_t = 0$

$t=\infty$, $q_t = q_e$

Obtained equation under the above boundary conditions:

$$q_t = q_e \left(1 - e^{\left(-k_f t\right)}\right) \qquad (S2)$$

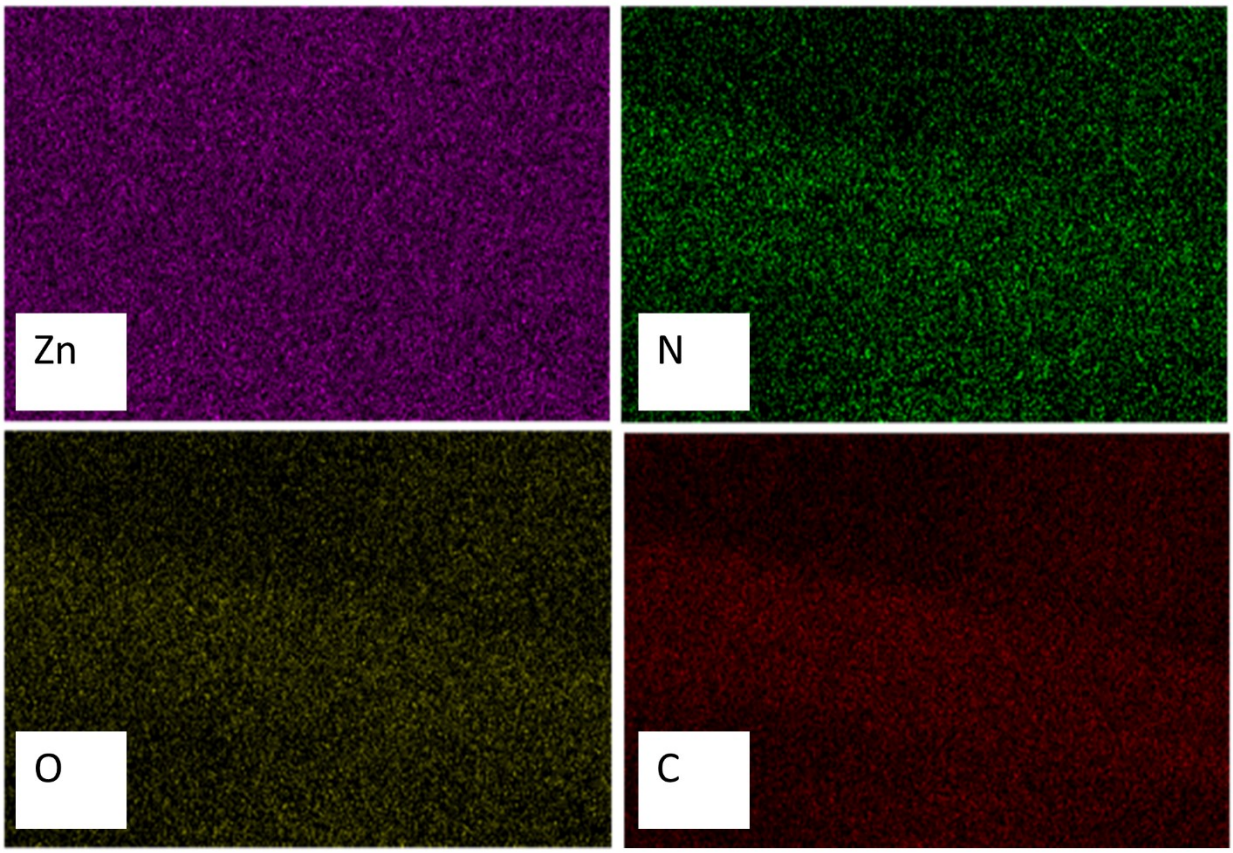

Figure S1. EDX mapping of CDA-silica@ZIF-8 NFA.

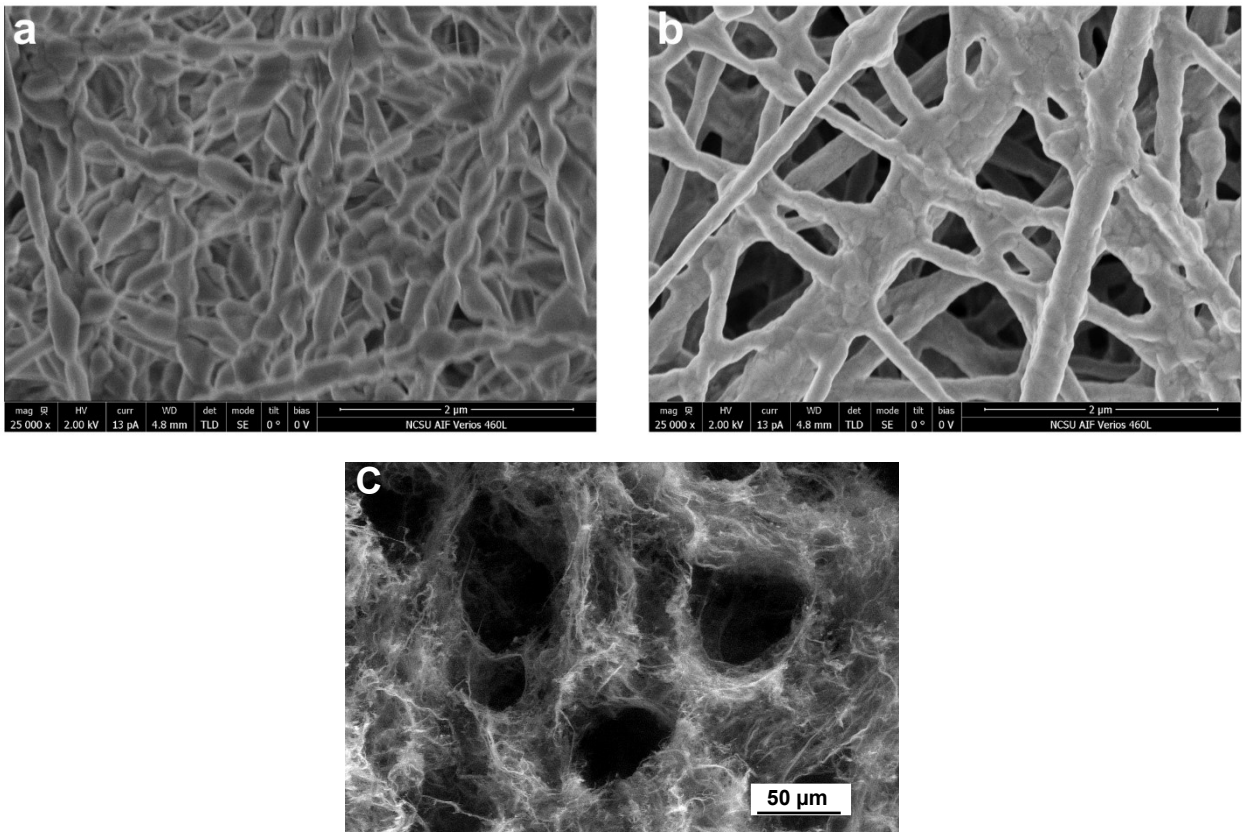

Figure S2. SEM images of a) CDA-silica@ZIF8-200cy and b) CDA-silica@ZIF8-300cy NFAs and (c) CDA-silica coated with 120cy of ZnO.

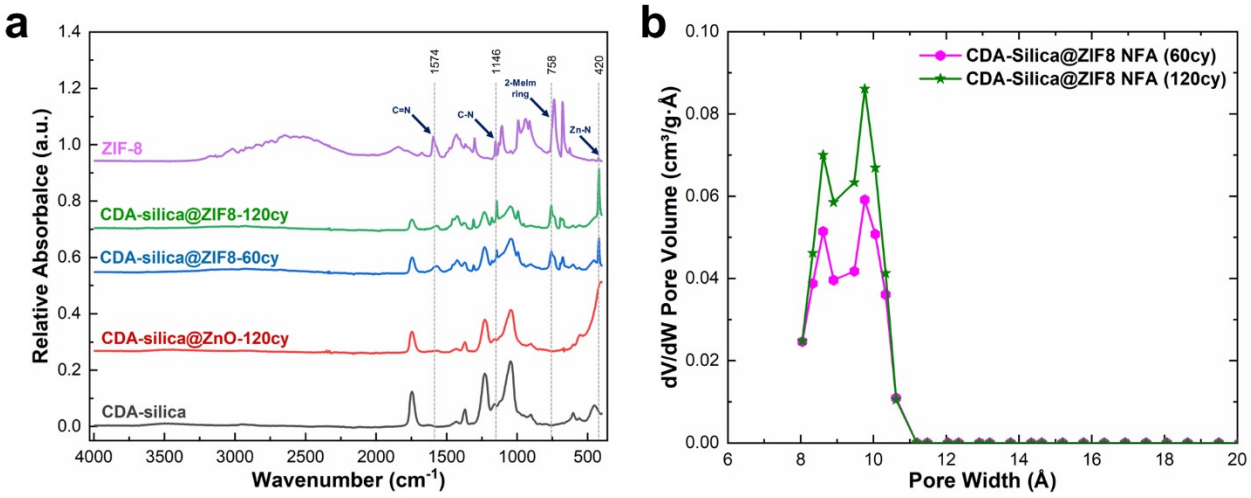

Figure S3. a) FTIR spectra of CDA-silica, ZnO coated CDA-silica and CDA-silica@ZIF-8 NFAs. Characteristic IR peaks at 1574 cm^{-1}, 1146 cm^{-1}, 758 cm^{-1}, and 420 cm^{-1}, corresponding to aromatic C=N, C-N, out-of-plane bending of the 2-MeIm ring, and Zn-N stretching modes of ZIF-8, respectively are shown. b) pore size distribution of ZIF-8 in the CDA-silica@ZIF-8 NFAs.

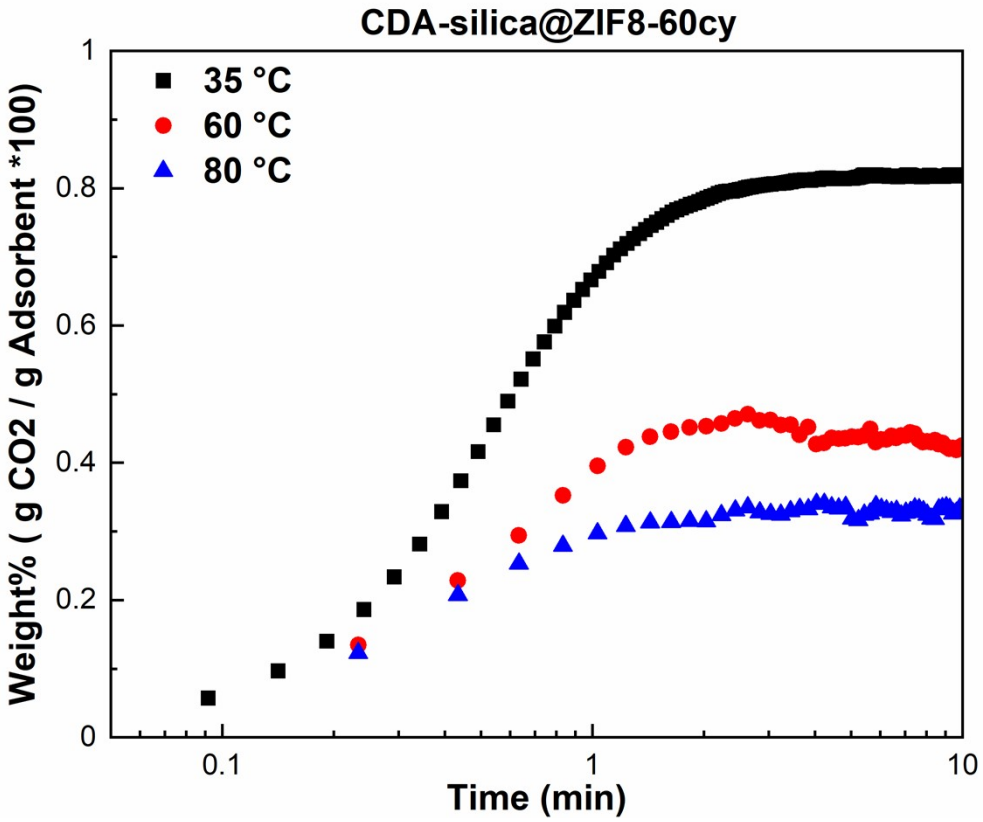

Figure S4. CO_2 uptake of CDA-Silica@ZIF8-60cy at 35, 60 and 80 °C.

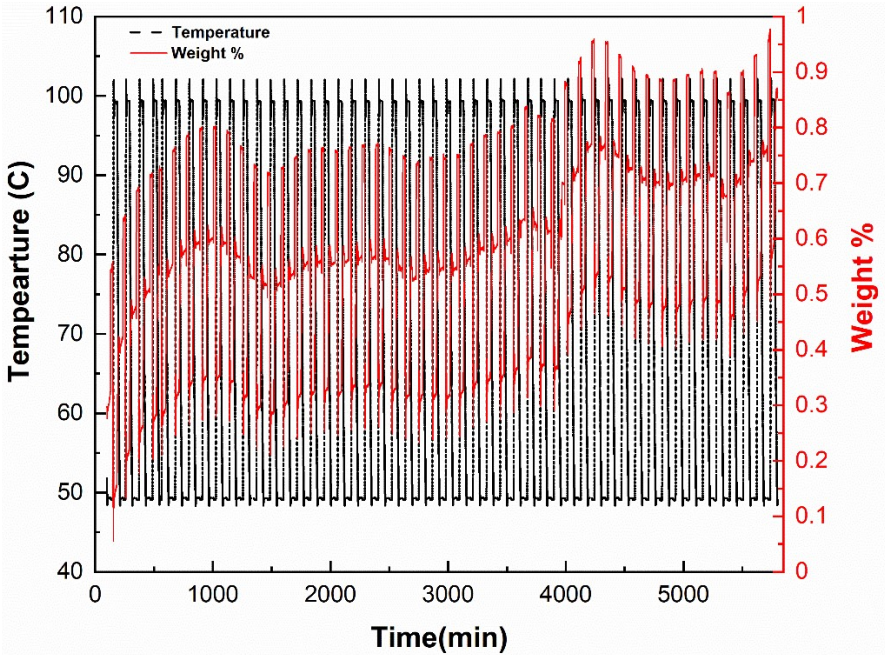

Figure S5. Cyclic CO_2 uptake of CDA-Silica@ZIF8-12cy at 50 °C using CO_2/N_2 (15/85) via a gravimetric method.

Table S1- Kinetic parameters of pseudo-first order Model

Sample	T (°C)	q_{exp} (mmol/g)	K_f (min^{-1})	q_e (mmol/g)
CDA-Silica@ZIF8-120cy NFA	35	4.04	1.3642	1.61
CDA-Silica@ZIF8-60cy NFA	35	2.36	2.1439	1.984
CDA-Silica NFA	35	1.002	2.7547	0.89

Table S2- Copper removal performance of various ZIF-8 based composites

Synthesis Method	**Adsorbents**	**Adsorption Capacity (mg/g)**	**Reference**
Solvothermal	Cellulose /ZIF-8 aerogels	270.2	[8]
	Cellulose nanofiber/chitosan/montmorillonite aerogel	182.98	[9]
	Fe_3O_4/ZIF-8 nanocomposite powder	21.1	[10]
	ZIF-8 membrane on alumina hollow fiber	76.5	[11]
	Fe_3O_4@Carbon@ZIF-8 Nanoparticles	234.7	[12]
	Chitosan-ZIF-8 beads	165.7	[13]
Vapor phase	CDA-silica@ZIF8 NFA	248.4	This work

References:

1 Y. Si, J. Yu, X. Tang, J. Ge and B. Ding, *Nat. Commun.*, 2014, **5**, 5802.

2 T. Pirzada, Z. Ashrafi, W. Xie and S. A. Khan, *Adv. Funct. Mater.*, 2020, **30**, 1907359.

3 D. T. Lee, J. Zhao, G. W. Peterson and G. N. Parsons, *Chem. Mater.*, 2017, **29**, 4894–4903.

4 M. Du, L. Li, M. Li and R. Si, *RSC Adv.*, 2016, **6**, 62705–62716.

5 S. Kaur, S. Rani, R. K. Mahajan, M. Asif and V. K. Gupta, *J. Ind. Eng. Chem.*, 2015, **22**, 19–27.

6 S. Loganathan, M. Tikmani, S. Edubilli, A. Mishra and A. K. Ghoshal, *Chem. Eng. J.*, 2014, **256**, 1–8.

7 F. Yang, X. Zhu, J. Wu, R. Wang and T. Ge, *Powder Technol.*, 2022, **399**, 117090.

8 T. Cheng, Y. Zhang, F. Cui, G. Jiang, P. Liu, J. Guo, K. Cui, C. Chen and H. Li, *Chem. Phys. Lett.*, 2022, **808**, 140100.

9 N. Rong, C. Chen, K. Ouyang, K. Zhang, X. Wang and Z. Xu, *Sep. Purif. Technol.*, 2021, **274**, 119120.

10 Q. Wu, D. Wang, C. Chen, C. Peng, D. Cai and Z. Wu, *J. Environ. Manage.*, 2021, **290**, 112626.

11 D. N. binti Awang Chee, F. Aziz, A. F. Ismail, M. A. bin Mohamed Amin and M. S. Abdullah, *J. Environ. Chem. Eng.*, 2021, **9**, 105343.

12 Z. Xiong, H. Zheng, Y. Hu, X. Hu, W. Ding, J. Ma and Y. Li, *Sep. Purif. Technol.*, 2021, **277**, 119053.

13 C. Wang, Q. Sun, L. Zhang, T. Su and Y. Yang, *J. Environ. Chem. Eng.*, 2022, **10**, 107911.